Mott insulator phases of nonlocally coupled bosons in bilayer optical superlattices

Sayan Lahiri [◉],[1] Suman Mondal [◉],[1] Manpreet Singh,[1,2] and Tapan Mishra [◉][1]

[1]*Department of Physics, Indian Institute of Technology, Guwahati 781039, India*
[2]*Laboratoire Matériaux et Phénomènes Quantiques, CNRS, Université de Paris, 75013 Paris, France*

We investigate the ground-state properties of a nonlocally coupled bosonic system in a bilayer optical superlattice by considering bosons in one layer to be of soft core in nature and separately allowing two- and three-body hard-core constraints on the other layer. We find that the presence of different constraints on bosons in one layer influences the overall phase diagram exhibiting various Mott insulator phases at incommensurate densities due to the presence of the superlattice potential apart from the usual Mott insulators at commensurate densities. Moreover, the presence of two- or three-body constraints significantly modifies the Mott insulator to superfluid phase transition points as a function of the superlattice potential. Due to the various competing interactions, constraints, and superlattice potential, the phase diagrams exhibit significantly different features. We obtain the complete phase diagrams by using the cluster mean-field-theory approach. We further extend this work to a coupled two-leg ladder superlattice where we obtain similar physics using the density-matrix renormalization-group method.

I. INTRODUCTION

Quantum phase transitions in systems of ultracold quantum gases in optical lattices have revealed a host of new phenomena in recent years. The rapid progress in experimental manipulation of these weakly interacting systems in optical lattices has revealed various interesting physics which was impossible to understand using the conventional solid-state systems. One such example is the observation of the superfluid (SF) to Mott insulator (MI) phase transition in a three-dimensional optical lattice [1], a phenomenon which was predicted in the context of the Bose-Hubbard model [2,3]. The state-of-the-art experimental setups and the flexibility to control the system parameters in such systems have provided a new platform to explore interesting phenomena in nature which has led to a plethora of novel and exciting physics. While the dominant interaction in such ultracold systems is the two-body contact interaction, it has been shown that there exist higher-order local interactions as well, which have non-negligible effects on the ground-state properties [4,5]. Recently it was shown that the leading multibody interactions, such as the three-body interaction, can be engineered under suitable conditions in optical lattices [6–9], which can play important roles in discovering many-body-induced quantum phases, especially at higher densities [10–17]. Such many-body interactions can drastically modify the behavior of the system. For instance, the three-body interaction can become very large, leading to the three-body hard core constraint where no more than two particles can occupy a single site. This feature is crucial in studying the systems of attractive bosons in optical lattices by preventing the collapse of bosons. These three-body constrained bosons (TCBs) are shown to exhibit the superfluid to pair-superfluid phase transition in optical lattice [18]. A similar situation is also seen in the regime of large on-site two-body repulsion where no two bosons can simultaneously occupy a single site. In such a situation the bosons are called hard-core bosons (HCBs) or a Tonks gas [19].

On the other hand, long-range dipolar interactions in atoms, molecules, and Rydberg atoms have culminated into a completely new realm of physics where several novel phenomena have been predicted and observed in recent experiments such as charge-density wave phases, exotic supersolid phases, and self-bound quantum droplets [20–24]. Interestingly, these nonlocal interactions have been shown to couple systems which are spatially separated from each other such as the bilayer systems and two-leg ladders. In such a scenario one can drive the two decoupled systems together with the help of the long-range dipole-dipole interaction [25–28]. Moreover, the bilayer systems with interlayer interactions resemble systems of two-component atomic mixtures in optical lattices. A new area of research has evolved in the context of the dual-species bosons, fermions, and Bose-Fermi mixtures due to the recent advancement in cooling and trapping of binary mixtures in experiments [29–38]. The creation and manipulation of such dual-species mixtures with two completely different species of atoms or two hyperfine states of a particular species in optical lattices to achieve strong correlations have opened up various avenues in addressing complex many-body systems. The presence of different types of interactions compared to the single-species systems has made the binary mixture a topic of great interest; as a result, several theoretical predictions and experimental observations have been made in various context [33,35–37,39–49]. At the same time, the creation of optical superlattices [50,51] has proven to provide an additional flexibility to manipulate lattice potentials and periodicity, which results in different interesting applications. A great deal of research has been done on optical superlattices and several new phases have been predicted in theory
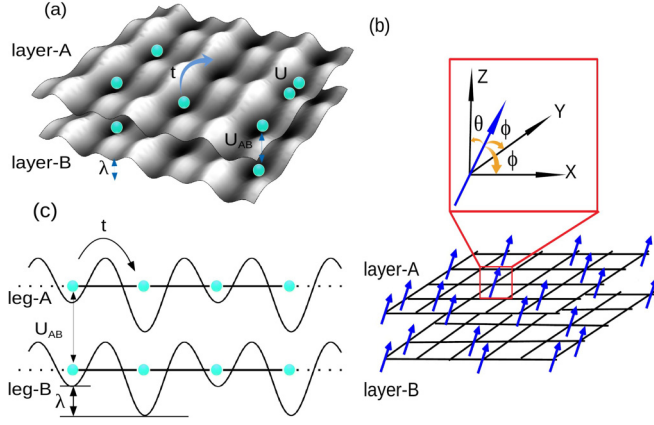
FIG. 1. (a) Illustration of a bilayer superlattice having periodicity equal to 2, showing the intralayer and interlayer interactions. (b) Possible alignment of the dipoles in this bilayer system. The inset shows one dipole placed in the origin in such a way that it makes an angle ϕ with the x and y axes and θ with the z axis. (c) Two-leg optical superlattice with leg A and leg B containing the soft-core bosons and constrained bosons, respectively. These two legs interact with each other via the nonlocal interaction U_{AB}.

and observed in experiments in various context [14,50–61]. Although various investigations have been made in systems of ultracold quantum gases in optical superlattices, the study of bilayer superlattices or binary mixtures in superlattices may lead to novel phenomena. As the systems of a dual-species mixture can be mapped to the spin systems under proper conditions, it promises a direct connection to the many-electron systems and magnetism [62]. One such recent study of multicomponent bosons in optical superlattices has predicted various gapped phases using the single-site mean-field approximation where the bosons are assumed to be soft core in nature and the intraspecies interactions are considered to be of identical strength [63]. As a result, the influence of one species of atoms on the other and vice versa is similar in nature.

At this point we consider a bilayer bosonic system in an optical superlattice as depicted in Fig. 1(a). The construction of the bilayer system is in such a way that both layers are identical to each other in terms of lattice translation and a two-period superlattice potential is present only in the x direction. As a result, the lattice periodicity is doubled in the x direction, whereas in the y direction there is no change in the periodicity. In principle, one can consider the superlattice potential in both directions, which is expected to exhibit similar particle dynamics in both directions. However, the choice made in this work provides a situation where the particles tend to localize in every alternate site due to the superlattice potential in one direction, whereas they are free to move in the other direction. In such a system we consider the bosons in layer A to be soft core in nature, whereas bosons in layer B experience two- or three-body hard-core constraint.

We assume the particles are dipolar in nature in both layers and there exist only interlayer interactions with the intralayer interactions being suppressed. This situation can be achieved by orienting the dipoles in such a way that they are at magic angles with the line joining two nearest-neighbor dipoles in

both the x and y directions of the layer. In such a scenario, the angle made with the line joining the dipoles sitting in two different layers is different from the magic angle resulting in a finite repulsive interaction which is proportional to $1 - 3\cos^2\theta$, as depicted in Fig. 1(b). Moreover, the distance between the layers can also be varied to tune the interlayer interaction. Since intralayer (contact) and interlayer (long-range) interactions originate from different physical phenomena, it is possible to tune them independently. The model which describes such a system is the modified Bose-Hubbard model given as

$$
\begin{aligned}
H = {} & -t \sum_{\langle i,j \rangle, \sigma \in [A,B]} (a_{i\sigma}^\dagger a_{j\sigma} + \text{H.c.}) \\
& + \sum_{i,\sigma \in [A,B]} \left[\frac{U_\sigma}{2} n_{i\sigma}(n_{i\sigma} - 1) - (\mu_\sigma - \lambda_i)n_{i\sigma} \right] \\
& + \frac{W_\sigma}{6} \sum_{i,\sigma \in [A,B]} n_{i\sigma}(n_{i\sigma} - 1)(n_{i\sigma} - 2) \\
& + U_{AB} \sum_i n_{iA} n_{iB}.
\end{aligned}
\tag{1}
$$

Here $a_{i\sigma}^\dagger$ ($a_{i\sigma}$) is the creation (annihilation) operator which creates (destroys) a boson in layer σ ($=A, B$) and at site i, $n_{i\sigma} = a_{i\sigma}^\dagger a_{i\sigma}$ is the number operator, and t is the hopping amplitude between any two nearest-neighbor sites i and j. While U_σ represents the local two-body intralayer interactions, W_σ represents the local three-body intralayer interactions and U_{AB} represents the interlayer two-body interaction. In addition, μ_σ is the chemical potential and λ_i is the superlattice potential in the x direction, which is 0 (λ) for odd (even) site indices, as shown in Fig. 1(a). The two- and three-body constraints in layer B are achieved by considering $(a^\dagger)^2 = 0$ and $(a^\dagger)^3 = 0$, respectively. Note that for the HCBs in layer B, $U_{\sigma=B} \to \infty$ and the terms associated with $U_{\sigma=B}$ will vanish in the model (1) due to the hard-core constraint. It should be noted that the presence of a finite local three-body interaction mainly modifies the superfluid to Mott insulator transition critical points, which has been investigated in detail in other works. Therefore, we discuss the case in which the contribution from either the three-body and higher-order terms is neglected in layer A. The three-body hard-core constraint is achieved by considering $W \to \infty$ in layer B. For a large superlattice potential each two-site unit cell can effectively behave like a single site. In such a scenario, depending on the number of particles in the deep site and the effective repulsive interaction, the on-site Wannier orbitals are affected, leading to effective modification of the tunneling and on-site interaction. However, in our calculations we do not include these modifications and limit our analysis to the standard Bose-Hubbard model.

The rest of the paper in organized as follows. In Sec. II we briefly discuss the method used in this work. Section III contains the results and a discussion of our work. We summarize in Sec. IV.

II. METHOD

We investigate the ground-state properties of the model given in Eq. (1) by considering soft-core bosons in layer A

and loading layer B with HCBs and TCBs separately in two different scenarios. In both cases we study the phase diagram of the system and obtain various gapped phases which appear at commensurate and incommensurate densities. We also show how the tip positions of these gapped phases or, in other words, the gapped to gapless phase transitions behave by changing the constraint on the bosons in layer B. To this end we implement the cluster mean-field theory (CMFT) approach to analyze Eq. (1). It should be noted that this problem can also be analyzed using the simple mean-field decoupling approximation [64], which can capture the qualitative physics of the system. However, in order to achieve better accuracy we employ the CMFT approach. For the models like the one shown in Eq. (1), the CMFT method works fairly well with less computational complexity and may approach in the thermodynamic limit the quantum Monte Carlo results for some specific situations [28,65,66]. In the end we investigate the scenario for the one-dimensional case to examine the fate of quantum phases in reduced dimension. In this regard, we utilize the well-known density-matrix renormalization-group (DMRG) method for the two-leg ladder model to examine the features in one dimension.

In the CMFT method the entire system is divided into identical clusters of a limited number of sites which can be treated exactly and then the coupling between different clusters is treated in a mean-field way. The accuracy of this method improves by increasing the number of sites in the cluster. With this approximation the original Hamiltonian of Eq. (1) can be written as

$$H = H_C + H_{\text{MF}}, \tag{2}$$

where H_C (H_{MF}) is the cluster (mean-field) part of the Hamiltonian. Here H_C is the same as in Eq. (1) but is limited to the cluster size. The hoppings between the clusters are then approximated using the simple mean-field-type decoupling scheme given as

$$a_{i\sigma}^{\dagger} a_{j\sigma} = \langle a_{i\sigma}^{\dagger} \rangle a_{j\sigma} + a_{i\sigma}^{\dagger} \langle a_{j\sigma} \rangle - \langle a_{i\sigma}^{\dagger} \rangle \langle a_{j\sigma} \rangle. \tag{3}$$

Introducing the two-layer-dependent SF order parameter $\psi_{i\sigma} = \langle a_{i\sigma}^{\dagger} \rangle = \langle a_{i\sigma} \rangle$ and using Eq. (3), we write the H_{MF} as

$$H_{\text{MF}} = -t \sum_{\sigma,\langle i,j \rangle} [(a_{i\sigma}^{\dagger} + a_{i\sigma})\psi_{j\sigma} - \psi_{i\sigma}^{*}\psi_{j\sigma}]. \tag{4}$$

In our calculation we have set $t = 1$ to make all the physical quantities dimensionless. For the CMFT calculation we use a four-site cluster which consists of two sites from both layers. We call this a supercell in the following discussion. We define the quantities $n = \sum_{\sigma \in [A,B]} \sum_{i=1}^{2} n_{i\sigma}$ and $\rho = \frac{1}{4}n$, which are the total particle number and density in one supercell to distinguish various phases. We also assume equal chemical potentials for bosons in both layers by setting $\mu_A = \mu_B = \mu$ in our calculation. By fixing the values of U_A, U_B (in the case of TCBs), and U_{AB} we compute the complete phase diagram in the μ/t vs λ/t plane. We also consider some specific value of λ and vary the interaction to obtain the phase diagram as done in Ref. [63]. Further, we analyze the system in one dimension by considering a two-leg ladder which can be viewed as two superlattice chains coupled via the dipole-dipole interaction. We study the model (1) by using
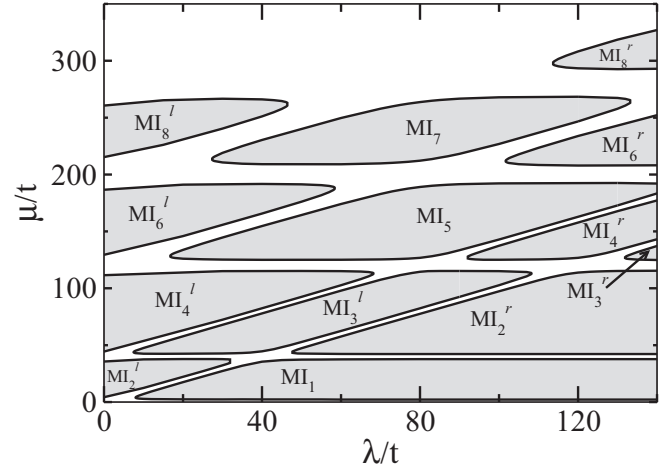

FIG. 2. The CMFT phase diagram when bosons in layer A are soft core and bosons in layer B are HCBs. Here $U_A = 80$ and $U_{AB} = 40$.

the DMRG method by considering σ as the two legs of the ladder. In our DMRG calculation we assume system sizes up to 100 sites and 500 density-matrix eigenstates. The cluster and system size considered in our calculation are found to be sufficient to capture the physics we are interested in.

III. RESULTS AND DISCUSSION

A. Hard-core constraint for bosons in layer B

In this section we discuss the case when the bosons in layer B are hard core in nature. In the decoupled layer limit, i.e., $U_{AB} = 0$, both layers behave as independent two-dimensional (2D) systems. It is well known that there exists a critical value of λ for which the system undergoes an SF to MI transitions at half filling for both hard-core and soft-core bosons in two dimensions [14,56,67]. Therefore, it is expected that the first Mott lobe would appear in the system after a critical value of λ for density $\rho = 1/4$ where either of the layers attains half filling. At this stage the interlayer interaction U_{AB} has no role in the phase diagram as the particles reside in either of the layers. However, with an increase in the chemical potential μ both layers get populated and one may see an interesting interplay between U_A, U_{AB}, and λ which leads to various gapped phases and transitions to the SF phase at different integer and noninteger fillings of individual layers, as shown in Fig. 2. In this paper we call all the gapped phases MI phases, although the ones at noninteger densities are different from the usual MI phase where each site is occupied with the same integer number of bosons [52]. However, in the case of superlattices, one can consider the density with respect to the unit cell (the periodicity of the superlattice) so that the gapped phases at noninteger densities can be called MI phases for those particular densities.

The phase diagram of Fig. 2 is obtained by self-consistently diagonalizing the Hamiltonian shown in Eq. (2) to obtain the ground-state wave function and then the super-fluid order parameter ψ as discussed in the preceding section. By considering a large on-site interaction $U_A = 80$ and $U_{AB} = U_A/2$ which is sufficient to establish various gapped phases
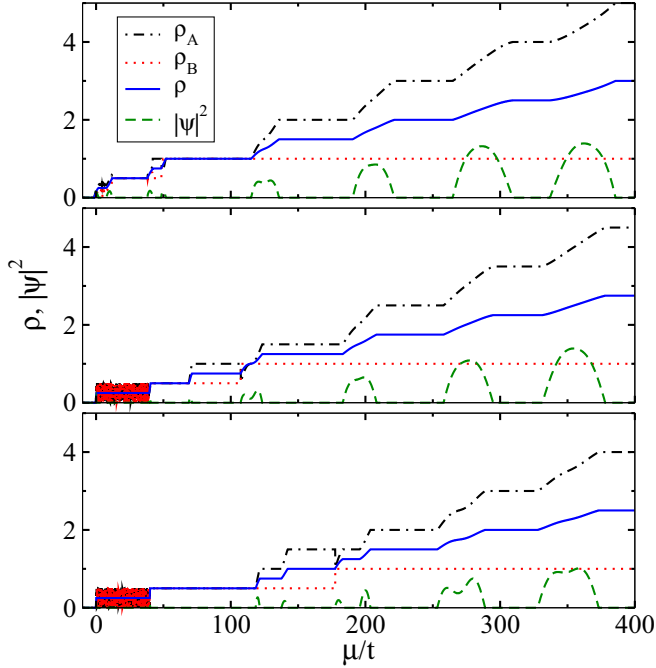
FIG. 3. Variation of ρ (solid blue curve) and $|\psi|^2$ (dashed green curve) with respect to μ/t for $\lambda = 10, 70, 140$ shows the gapped and gapless phases when layer B has HCBs. The plateaus in ρ correspond to the gap in the MI phases whereas the shoulders around the plateaus (where the values of $|\psi|^2$ are finite) indicate the gapless SF phase. We also plot the individual layer densities as ρ_A (dot-dashed curve) and ρ_B (dotted curve) for clarity. Due to the hard-core nature, ρ_B saturates at one. The fluctuations in ρ_A and ρ_B are due to the degenerate states in the CMFT calculation.

for the soft-core bosons in one layer and by varying λ for a wide range of values, we obtain the entire phase diagram which consists of the gapped MI lobes and the intermediate SF phases. Here we define the superfluid density $\rho_s = \frac{1}{4} \sum_{i,\sigma} |\psi_{i\sigma}|^2$, where $\psi_{i\sigma}$ is the layer-dependent superfluid order parameter as discussed in the preceding section. The gapped phases are obtained by looking up the regions in which the total superfluid density vanishes in the ρ_s vs μ/t plot for several values of λ. In Fig. 3 we show ρ (solid blue line) and ρ_s (dashed green line) with respect to μ/t for $\lambda = 10, 70, 140$, which cut through the gapped phases in Fig. 2 parallel to the μ/t axis. It can be seen that for a particular λ, as μ increases the plateaus in ρ appear and at the same time ρ_s vanishes corresponding to the MI phases. We denote the MI phases by MI_n, where the subscript n indicates the total number of particles, i.e., $n_A + n_B$ in a supercell. The possible supercell atom distribution for all the MI phases are presented in Table I.

It can be seen from Fig. 2 that the first lobe which corresponds to the MI_1 appears after a critical $\lambda \sim 8$ at $\rho = 1/4$, as discussed before. The gap continues to be finite and the lobe expands as λ increases further. Upon increasing the value of μ or, in other words, by increasing the particle number in the system, the other gapped phases start to appear, which are seen as plateaus in the ρ vs μ/t plot shown in Fig. 3. For total density $\rho = 1/2$ (half filling of both the layers), there exist two gapped lobes separated by the SF phase as a function of λ.

TABLE I. Boson distribution in the unit cell: various MI states when atoms in layer B are HCBs. Each state shows the density distribution in the supercell corresponding to a particular MI state for a given n and ρ.

n	ρ	Supercell configuration
1	0.25	$MI_1 = \begin{vmatrix} 0 & 1 \\ 0 & 0 \end{vmatrix}$ or $\begin{vmatrix} 0 & 0 \\ 0 & 1 \end{vmatrix}$
2	0.5	$MI_2^l = \begin{vmatrix} 0 & 1 \\ 1 & 0 \end{vmatrix}$ or $\begin{vmatrix} 1 & 0 \\ 0 & 1 \end{vmatrix}$ and $MI_2^r = \begin{vmatrix} 0 & 1 \\ 0 & 1 \end{vmatrix}$
3	0.75	$MI_3^l = \begin{vmatrix} 1 & 1 \\ 0 & 1 \end{vmatrix}$ and $MI_3^r = \begin{vmatrix} 0 & 2 \\ 0 & 1 \end{vmatrix}$
4	1.0	$MI_4^l = \begin{vmatrix} 1 & 1 \\ 1 & 1 \end{vmatrix}$ and $MI_4^r = \begin{vmatrix} 1 & 2 \\ 0 & 1 \end{vmatrix}$
5	1.25	$MI_5 = \begin{vmatrix} 1 & 2 \\ 1 & 1 \end{vmatrix}$
6	1.5	$MI_6^l = \begin{vmatrix} 2 & 2 \\ 1 & 1 \end{vmatrix}$ and $MI_6^r = \begin{vmatrix} 1 & 3 \\ 1 & 1 \end{vmatrix}$
7	1.75	$MI_7 = \begin{vmatrix} 2 & 3 \\ 1 & 1 \end{vmatrix}$
8	2.0	$MI_8^l = \begin{vmatrix} 3 & 3 \\ 1 & 1 \end{vmatrix}$ and $MI_8^r = \begin{vmatrix} 2 & 4 \\ 1 & 1 \end{vmatrix}$

The appearance of a large gap at vanishing λ can be attributed to the effect of U_{AB} which prevents the atoms in layer A and layer B from occupying the same sites. Hence, one may expect a gapped phase which is similar to the checkerboard solid for the Bose-Fermi mixture on a square lattice [68]. We call this phase the MI_2^l phase. As discussed in Ref. [68], the stability of this gapped phase depends on the ratio U_{AB}/U_A. In our case $U_{AB}/U_A = 0.5$, which is sufficient to open a gap in the system. However, the gap gradually decreases as the value of λ increases and as a result the system enters the SF phase. This is because of the increase in the effective on-site potential on every alternate site in both layers which results in a smaller ratio U_{AB}/U_A. Increasing the value of λ further, the gapped phase reappears after a critical $\lambda \sim 47.6$. At this stage, the superlattice potential is very strong compared to the ratio U_{AB}/U_A and the bosons reside in the deep lattice sites. We call this gapped phase the MI_2^r phase, which is similar to the striped phase for the 2D case. The density distribution can be seen from the ρ vs μ/t plot shown in Fig. 3 (see the figure for details).

At this stage a further increase in density results in the next gapped phases at $\rho = 3/4$. The situation at this density is completely different from the case of half density. Here we find that the system is initially in the gapless SF phase for a range of λ starting from $\lambda = 0$ and there exists a gapped island for some intermediate range of λ and then a gapped phase for large values of λ. The physics at this density can be understood by the following analysis. For $\lambda = 0$, as μ increases layer A will start to get populated first due to the soft-core nature and all the sites are occupied by one atom each, giving rise to unit filling and layer B remains at half filling. At unit filling layer A is in the MI phase as U_A is sufficiently strong. As a result, the atoms in layer B will experience equal repulsion U_{AB} from all the sites of layer A and hence they can move freely, giving rise to the SF phase of layer B. Therefore, the system as a whole is gapless,

although layer A is in the MI state. The increase in λ, however, introduces the gap in the system by localizing the hard-core bosons in the deep sites of layer B while layer A remains in the MI phase. The resulting system is therefore a gapped phase. This phase is called the MI_3^l phase, which lies between $\lambda \sim 7.5$ and $\lambda \sim 108.4$. A further increase in λ leads to an increase in particle-hole fluctuation and the gapped MI phase starts to melt and the SF phase reappears in the system. Eventually, the system enters another gapped phase after a critical value of $\lambda \sim 131.10$, where in layer A two bosons are localized in the deep lattice sites. We call this phase the MI_3^r phase, as depicted in the phase diagram of Fig. 2.

At this stage, a further increase in the value of μ will facilitate the addition of bosons in layer B, which saturates at unit filling due to the hard-core nature of bosons where all the sites are occupied by one boson each. This situation corresponds to the MI_4 phases in the phase diagram where the total density of the system is $\rho = 1$. When λ is small, we have every site in both layers occupied by one atom each and this phase is called the MI_4^l. When λ increases, the MI_4^l phase melts and the system enters the SF phase, eventually leading to the MI_4^r phase, where the atoms in layer A occupy the deep sites while layer B maintains uniform density due to the hard-core nature. In such a situation layer A is like the striped phase and layer B is saturated. These features can be clearly seen from the individual layer densities as shown in Fig. 3.

A similar situation arises for the other integer and noninteger densities where two distinct gapped phases appear at the two limits of the superlattice potential which are separated by the SF phase as depicted in the phase diagram of Fig. 2. The corresponding boson distributions are shown in Table I for clarity. For quarter-integer densities, the gapped islands appear for a range of intermediate values of λ separated by the SF phase. It should be noted that the tips of the right lobes shift towards larger values of λ as ρ increases. However, an interesting pattern occurs for the left lobes where the tip first shifts towards larger λ up to MI_4^l and then shifts left for higher densities. The appearance of this feature is attributed to the presence of bosons in layer B on all the lattice sites after a critical density $\rho \geqslant 1$. At these densities, the bosons in layer A are not affected by the presence of the bosons in layer B as they experience uniform repulsion which is equal to U_{AB} from all sites. Therefore, the physics of the system is governed only by the properties of bosons in layer A, as discussed in Ref. [14]. The MI^l-SF transition happens for smaller and smaller values of λ as the density increases because the increase in density leads to the decrease in effective on-site interactions on the shallow lattice sites. Therefore, the MI^l lobes melt into the SF phases due to the hopping t which dominates over the interactions. On the other hand, the SF-MI^r transition points shift towards larger values of λ at higher densities because of the increase in the number of particles in the deep wells which results in an increase in U_{AB}. Therefore, a stronger λ is necessary to introduce the MI^r phases as can be seen from the phase diagram.

To further understand the role of various interactions in our model, we study the phase diagram in the μ/t vs U/t plane as well. For this purpose we consider a cut across the phase diagram of Fig. 2 at $\lambda = 60$, which corresponds to
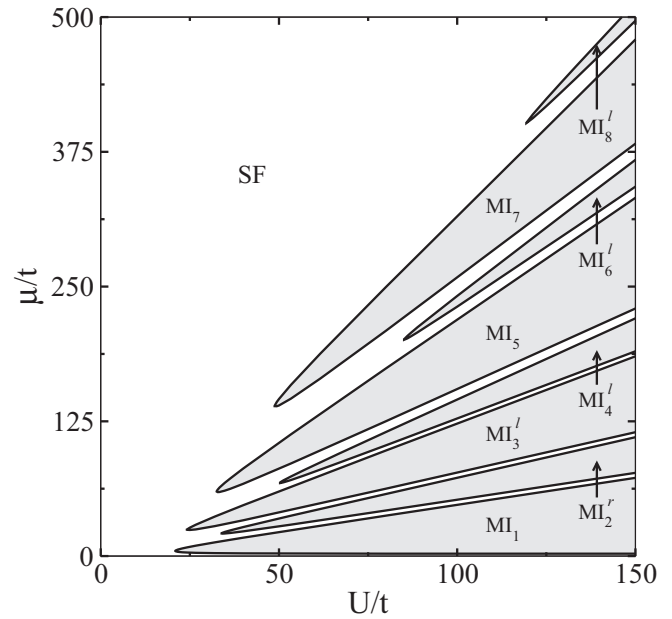

FIG. 4. The CMFT phase diagram in the μ/t vs U/t plane when bosons in layer A are soft core and bosons in layer B are hard core in nature. Here $U_A = U = 80$, $U_{AB} = 40$, and $\lambda = 60$. Since U_A is fixed in the case, we vary t in order to tune the ratio U/t.

$U = 80$ and $U_{AB} = 40$. In this case we vary t to obtain a range of U/t ratios and the resulting phase diagram in this case is shown in Fig. 4. We obtain a very interesting pattern of staggered MI lobes in this case. It can also be seen that the size of the MI lobes with odd integers in the subscript is larger than the MI lobes with even integers in the subscript. We follow the nomenclature of density distributions given in Table I and discuss the phase diagram in the following text. As we increase μ (from bottom to top) the particle number increases and there are two possibilities for each newly added particle: (i) It is added on top of a density distribution wherein the particle arrangement is identical in both the layers, that is, vacuum state MI_2^l, MI_4^l, MI_6^l, and MI_8^l, or (ii) the particle is added on top of an uneven density configuration, that is, MI_1, MI_3^l, MI_5, and MI_7. In case (i), the particle always ends up in the deeper potential well with fewer particles. Such a rearrangement is expected, as the value of the superlattice potential λ is sufficiently large. In case (ii), the particle entering the system avoids the densely occupied sites and prefers a site with lower occupancy. In this manner the contribution from the U and U_{AB} terms is minimized and the system tends to attain a more uniform density distribution. The lobes with an even density distribution are less stable compared to the lobes with an uneven density distribution and readily accept a new particle. Consequently, lobes of the former type are smaller in size with respect to the latter.

B. Three-body constraint for bosons in layer B

Now we discuss the case in which we replace the bosons in layer B with the TCBs. As discussed before, the effect of the three-body constraint is a result of large three-body on-site repulsion, i.e., $W \to \infty$. In such a situation the maximum
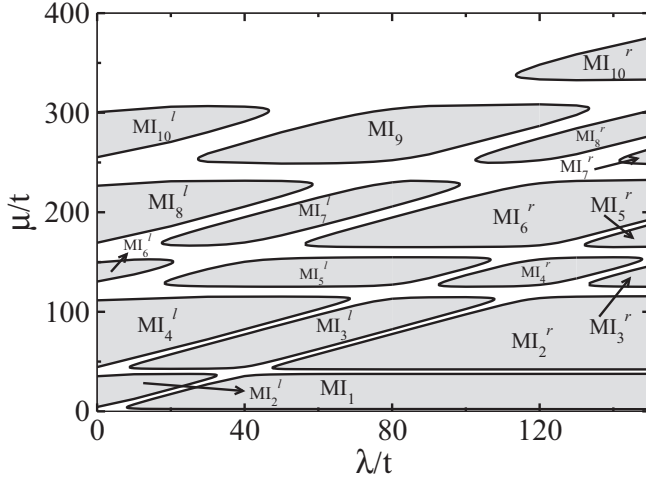
FIG. 5. The CMFT phase diagram when bosons in layer A are soft core and bosons in layer B are TCBs. Here $U_A = U_B = 80$ and $U_{AB} = 40$.

number of bosons allowed per lattice site is 2, i.e., $(a^\dagger)^3 = 0$. Such constrained bosons may impart significant effects on the overall phase diagram of bosons in the optical superlattice. Note that, in this case, we have finite values of the two-body interaction U_B in layer B. Similar to the preceding section, we numerically solve the mean-field Hamiltonian given in Eq. (2) and with $U_A = U_B = 80$, $U_{AB} = 40$, and varying λ we obtain various gapped phases. The ground-state phase diagram is shown in Fig. 5 and the particle distributions are shown in Table II.

It can be seen that the phase diagram for this case exhibits distinct features along with some similarities compared to the one obtained when bosons in layer B were hard core in nature

(compare with Fig. 2). Although the appearance of the MI phases for the odd (total) densities show similar behavior to the previous case, the even lobes exhibit different features with respect to their tip positions. It can be easily seen that the features in the part of the phase diagram from $n = 6$ onward match well with the phase diagram of the previous case (when layer B was hard core) except the first lobe at $n = 1$ of Fig. 2. This can be understood as follows. Let us consider the $\lambda = 0$ case for simplicity. As layer B is occupied by TCBs now, for $n = 6$ the density of the supercell is 1.5. This means there are two extra particles on top of the $\rho = 1$ lobe (MI$_4^l$). At $\rho = 1$, each site of both layers is occupied by one particle because of large on-site interactions U_A and U_B. Therefore, any extra particle which gets added to layer B containing the TCBs will behave like a hard-core boson on top of the uniform particle distribution. Hence, the effective system becomes equivalent to the one considered in the preceding section. However, there exist different gapped phases in low-density regimes, i.e., up to $n = 6$ lobes. For $n = 1$ ($\rho = 0.25$) we get an MI$_1$ phase which is similar to the one in Fig. 2, which starts after a finite value of $\lambda \sim 8$. As the number of particles increases, the second gapped phase MI$_2^l$ appears at $n = 2$ ($\rho = 0.5$) for $\lambda = 0$ and this survives up to a critical value of $\lambda \sim 32$; after this the system becomes gapless. In this case, each layer is occupied by one boson. A further increase in λ leads to the MI$_2^r$ phase, where the particles exist in the deep sites. Similarly, the MI$_4$ phases appear for $n = 4$ ($\rho = 1$) in the beginning when $\lambda = 0$ and the system is a proper Mott insulator at unit filling. An increase in λ will melt the gap and the SF phase appears; a further increase in λ will reintroduce the gap and the system gets into the MI$_4^r$ phase. In this phase, there can be two possible particle distributions in the lattice where two particles populate the deep sites of layer A, while sites of layer B are uniformly filled by one particle in each site

TABLE II. Boson distribution in the unit cell: various MI states when atoms in layer B are TCBs. Each state shows the density distribution in the supercell corresponding to a particular MI state for a given n and ρ.

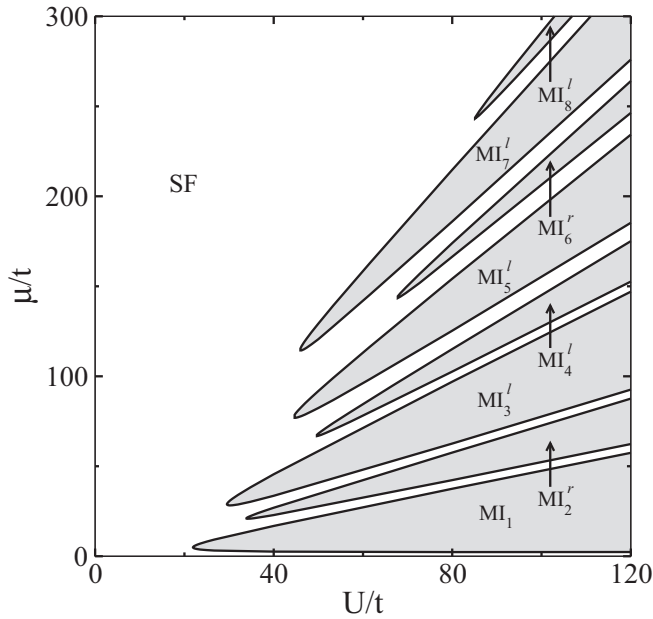| n	ρ	Supercell configuration
1	0.25	$\mathrm{MI}_1 = \left\lvert \begin{smallmatrix} 0 & 1 \\ 0 & 0 \end{smallmatrix} \right\rangle$ or $\left\lvert \begin{smallmatrix} 0 & 0 \\ 0 & 1 \end{smallmatrix} \right\rangle$
2	0.5	$\mathrm{MI}_2^l = \left\lvert \begin{smallmatrix} 0 & 1 \\ 1 & 0 \end{smallmatrix} \right\rangle$ or $\left\lvert \begin{smallmatrix} 1 & 0 \\ 0 & 1 \end{smallmatrix} \right\rangle$ and $\mathrm{MI}_2^r = \left\lvert \begin{smallmatrix} 0 & 1 \\ 0 & 1 \end{smallmatrix} \right\rangle$
3	0.75	$\mathrm{MI}_3^l = \left\lvert \begin{smallmatrix} 1 & 1 \\ 0 & 1 \end{smallmatrix} \right\rangle$ or $\left\lvert \begin{smallmatrix} 0 & 1 \\ 1 & 1 \end{smallmatrix} \right\rangle$ and $\mathrm{MI}_3^r = \left\lvert \begin{smallmatrix} 0 & 2 \\ 0 & 1 \end{smallmatrix} \right\rangle$ or $\left\lvert \begin{smallmatrix} 0 & 1 \\ 0 & 2 \end{smallmatrix} \right\rangle$
4	1.0	$\mathrm{MI}_4^l = \left\lvert \begin{smallmatrix} 1 & 1 \\ 1 & 1 \end{smallmatrix} \right\rangle$ and $\mathrm{MI}_4^r = \left\lvert \begin{smallmatrix} 0 & 2 \\ 0 & 2 \end{smallmatrix} \right\rangle$ or $\left\lvert \begin{smallmatrix} 1 & 2 \\ 1 & 1 \end{smallmatrix} \right\rangle$
5	1.25	$\mathrm{MI}_5^l = \left\lvert \begin{smallmatrix} 1 & 2 \\ 1 & 1 \end{smallmatrix} \right\rangle$ and $\mathrm{MI}_5^r = \left\lvert \begin{smallmatrix} 1 & 2 \\ 0 & 2 \end{smallmatrix} \right\rangle$
6	1.5	$\mathrm{MI}_6^l = \left\lvert \begin{smallmatrix} 2 & 1 \\ 2 & 1 \end{smallmatrix} \right\rangle, \left\lvert \begin{smallmatrix} 1 & 2 \\ 1 & 2 \end{smallmatrix} \right\rangle, \left\lvert \begin{smallmatrix} 2 & 1 \\ 1 & 2 \end{smallmatrix} \right\rangle$, or $\left\lvert \begin{smallmatrix} 1 & 2 \\ 2 & 1 \end{smallmatrix} \right\rangle$ and $\mathrm{MI}_6^r = \left\lvert \begin{smallmatrix} 1 & 2 \\ 1 & 2 \end{smallmatrix} \right\rangle$
7	1.75	$\mathrm{MI}_7^l = \left\lvert \begin{smallmatrix} 2 & 2 \\ 1 & 2 \end{smallmatrix} \right\rangle$ and $\mathrm{MI}_7^r = \left\lvert \begin{smallmatrix} 1 & 3 \\ 1 & 2 \end{smallmatrix} \right\rangle$
8	2.0	$\mathrm{MI}_8^l = \left\lvert \begin{smallmatrix} 2 & 2 \\ 2 & 2 \end{smallmatrix} \right\rangle$ and $\mathrm{MI}_8^r = \left\lvert \begin{smallmatrix} 1 & 3 \\ 2 & 2 \end{smallmatrix} \right\rangle$
9	2.25	$\mathrm{MI}_9 = \left\lvert \begin{smallmatrix} 2 & 3 \\ 2 & 2 \end{smallmatrix} \right\rangle$
10	2.5	$\mathrm{MI}_8^l = \left\lvert \begin{smallmatrix} 3 & 3 \\ 2 & 2 \end{smallmatrix} \right\rangle$ and $\mathrm{MI}_8^r = \left\lvert \begin{smallmatrix} 2 & 4 \\ 2 & 2 \end{smallmatrix} \right\rangle$

FIG. 6. The CMFT phase diagram in the μ/t vs U/t plane when bosons in layer A are soft core and bosons in layer B are three-body constrained. Here $U_A = U_B = U = 80$, $U_{AB} = 40$, and $\lambda = 60$. Since U_A is fixed in the case, we vary t in order to tune the ratio U/t.

and vice versa. This gapped phase vanishes at $\lambda \sim 148$ and a further increase in λ may lead to another gapped phase where the deep sites of both layers will be occupied by two particles (not in the range of λ considered here). The physics of odd integer lobes can also be understood from similar analogies discussed above.

Like before, in this case we also study the phase diagram in the μ/t vs U/t plane. The various parameter values are set as follows: $U_A = U_B = 80$, $U_{AB} = 40$, and $\lambda = 60$. The phase diagram obtained in this case is shown in Fig. 6 and it can be readily seen that it has features similar to those obtained previously in Fig. 4. Our discussion for the previous case holds mostly true in this case as well. However, there are two major differences between the two phase diagrams. (i) In the present case SF-MI transition critical points are in general higher than those found in the previous case. A straightforward explanation is that because of increased density fluctuations the SF region becomes enlarged and MI phase sets in relatively later. This can be seen by comparing the position of the tips of the MI$_1$ lobes in Figs. 4 and 6 (and other lobes as well). (ii) By introducing three-body constrained bosons in the present case, we allow more particles to accommodate in layer B and make room for more degenerate states to set in. This can be seen in Table II, in the density configurations for $n = 3, 6, \ldots$. This degeneracy has a significant effect on the phase diagram, as it tends to make the corresponding MI states less stable. If the reverse is true then we have stable MI phases, hence larger lobes.

C. Phase diagram in one dimension

In this section we complement our CMFT results presented above by analyzing the situation in one dimension. The one-
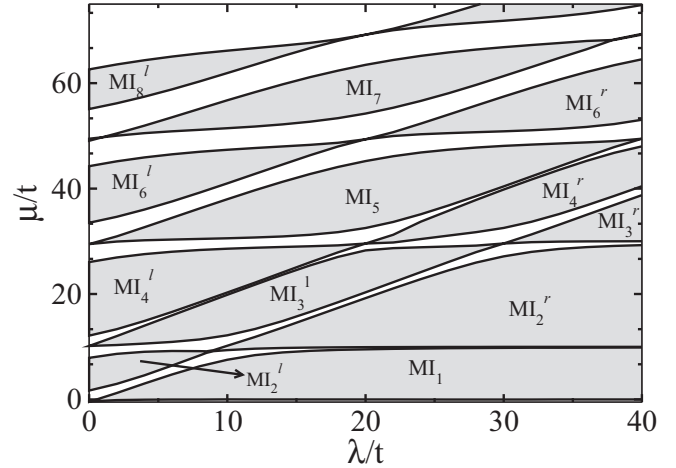

FIG. 7. The DMRG phase diagram when bosons in leg A are soft core in nature and bosons in leg B are HCBs.

dimensional analog of bilayer geometry is a two-leg ladder where layer A (B) is replaced by leg A (B) as shown in Fig. 1(c). The one-dimensional ladder geometry is extremely important in the context of condensed-matter systems as it resembles several structures of compounds of interest. The ladder geometry has been discussed in great detail in terms of the Hubbard model [69–81] and the Bose-Hubbard model [27,82–86]. Analogous to the 2D case, we assume only interleg dipole-dipole interactions by aligning the dipoles at a magic angle with each other along the leg direction. The physics of this system will be similar to the two-dimensional case due to the construction of the bilayer lattice in our case as discussed earlier. We employ the DMRG method to solve the model (1) in the canonical ensemble to compute the ground-state energy and wave function. To separate the gapped and gapless regions we calculate the single-particle gap, which is defined as

$$G_L = \mu^+ - \mu^-, \tag{5}$$

where $\mu^+ = E_L(N + 1) - E_L(N)$ and $\mu^- = E_L(N) - E_L(N - 1)$ are the chemical potentials, with $E_L(N)$ the ground-state energy of a system of length L and $N = N_A + N_B$ the total number of particles in the system. We obtain the ground-state phase diagram for both cases with bosons of leg B separately being HCBs and TCBs while bosons in leg A are soft core in nature and are shown in Fig. 7 ($U_A = 20$ and $U_{AB} = 10$) and Fig. 8 ($U_{A,B} = 20$ and $U_{AB} = 10$), respectively. One can easily see that the phase diagrams of Figs. 7 and 8 qualitatively match fairly well with the ones obtained using the CMFT method, i.e., Figs. 2 and 5, respectively. When bosons in leg B are HCBs, we observe that the MI tip positions first increase and then decrease as shown in Fig. 7, while there is an alternating increase and decrease of the tip positions when the bosons in leg B are TCBs as plotted in Fig. 8. The boundaries of the MI lobes are computed by extrapolating the μ values across the MI plateaus to the thermodynamic limit by quadratic fitting. In Fig. 9 we show the finite-size extrapolation of μ^+ (dashed lines) and μ^- (solid lines) for $\lambda = 18, 20, 22, 24, 26$. This clearly shows that $G_{L \to \infty}$ remains finite in the gapped phase and vanishes
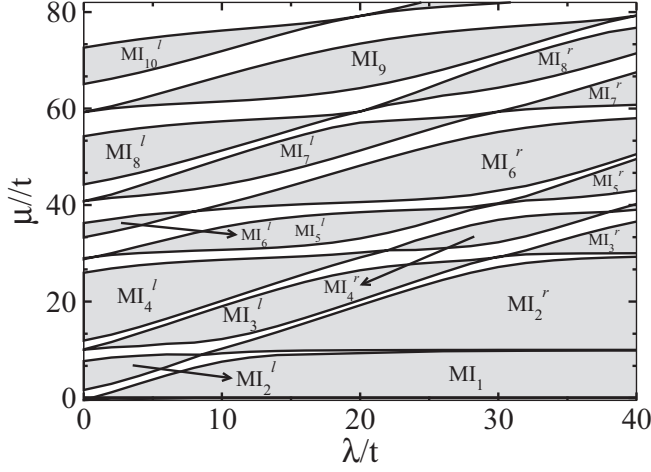
FIG. 8. The DMRG phase diagram when bosons in leg A are soft core in nature and bosons in leg B are TCBs.

in the gapless region, which clearly distinguishes between the gapped and gapless phases in the phase diagrams.

Further, to understand the particle distribution in real space we compute the expectation value of the number operator as

$$\langle n_i \rangle = \langle \Psi_0 | n_i | \Psi_0 \rangle, \tag{6}$$

where $|\Psi_0\rangle$ is the ground-state wave function of the system. As an example, in Fig. 10 we plot $\langle n_i \rangle$ with respect to the site index i for $\lambda = 12$ [Fig. 10(a)] and $\lambda = 28$ [Fig. 10(b)] corresponding to the MI_6^l and MI_6^r phases, respectively, of the phase diagram shown in Fig. 7. It can be clearly seen that for $\lambda = 12$ leg B is occupied by one hard-core boson in each site, whereas in leg A, each site is occupied by two atoms. However, for $\lambda = 28$, leg B is unaffected and leg A shows a $|\ldots 3131 \ldots\rangle$ type of distribution corresponding to the MI_6^r phase. A similar $\langle n_i \rangle$ vs i plot is shown in Fig. 11 for the MI_7 phase of Fig. 8. Here we consider $\lambda = 22$ [Fig. 11(a)]

FIG. 10. Density distribution of the system when (a) $\lambda = 12$ and (b) $\lambda = 28$ for $\rho = 1.5$ corresponding to the phase diagram of Fig. 7. The black circles and red squares represent the density distribution of leg A and leg B, respectively.

and 38 [Fig. 11(b)], which fall in two regions of the MI_7^l and MI_7^r phases, respectively. For $\lambda = 22$, all the sites of leg A are occupied by two particles each, whereas leg B exhibits a finite density oscillation corresponding to a $|\ldots 2121 \ldots\rangle$ type of distribution. However, for large $\lambda = 38$, the density distribution of leg A becomes $|\ldots 3131 \ldots\rangle$ while leg B remains unaffected. It should be noted that for the parameters considered here, the gapless regions between two gapped phases are very small compared to ones obtained using the CMFT method.

IV. CONCLUSION

We have analyzed the ground-state properties of a system of interacting bosons in a bilayer superlattice with interlayer
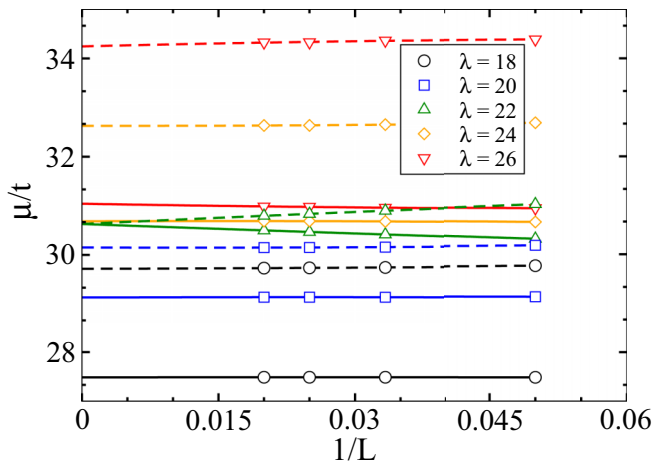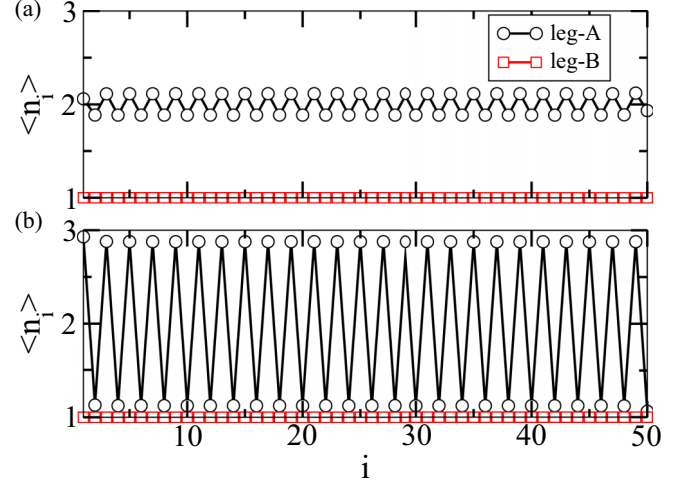

FIG. 9. Finite-size scaling of chemical potentials for $\rho = 1.5$ for different values of λ corresponding to the phase diagram of Fig. 7 when bosons in leg A are soft core in nature and bosons in leg B are HCBs. The solid and dashed lines represent the fitted functions to μ^+ and μ^-, respectively.
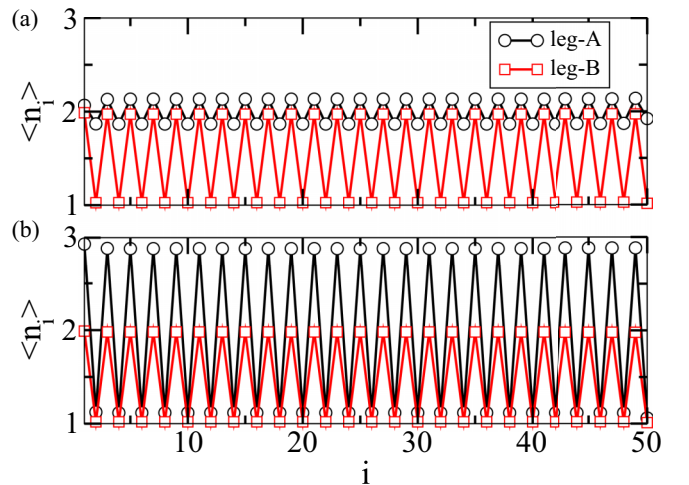

FIG. 11. Density distribution of the system when (a) $\lambda = 22$ and (b) $\lambda = 38$ for $\rho = 1.75$ corresponding to the phase diagram of Fig. 8. The black circles and red squares represent the density distribution of leg A and leg B, respectively.
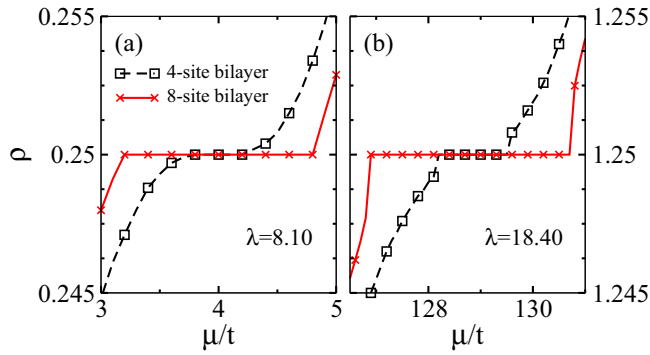
FIG. 12. Plots of ρ-μ for the cut along λ values (a) 8.1 and (b) 18.4, in the phase diagram given in Fig. 5. The four-site (eight-site) data are marked by the dashed line with black squares (solid line with red crosses). The plateaus represent the extent of Mott phases for the densities (a) 0.25 (MI_1) and (b) 1.25 (MI_5^l and MI_5^r). Some data points have been skipped for clarity.
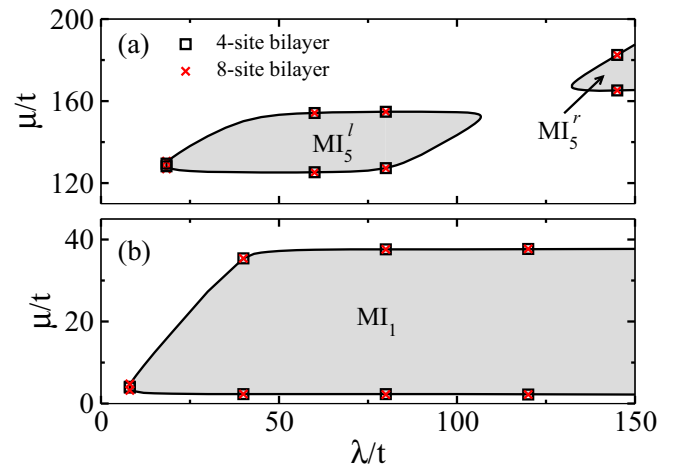

FIG. 13. Phase diagram indicating the Mott lobes in the λ-μ plane. The MI lobes correspond to the plateaus shown in (a) Fig. 12(a) and (b) Fig. 12(b). The four-site (eight-site) data are marked by black squares (red crosses).

repulsion which can be introduced by the dipole-dipole interactions. Considering the bosons in one layer as soft core in nature and separately allowing two- and three-body hard-core constraints in the other layer, we obtained the ground-state phase diagram using the CMFT approach. The phase diagrams exhibit various gapped MI phases at integer and half-integer densities. Due to the competition between the superlattice potential, intra- and interlayer interactions and the constraints on the bosons of layer B lead to interesting features in the phase diagram. Within the range of λ considered, we obtained two types MI lobes (MI_n^l and MI_n^r) separated by the SF region for a particular total number of particles in the supercell equal to n. Interestingly, when the hard-core constraint was applied in one layer, the tips of the MI_n^l lobes first shifted towards higher values of λ and then gradually receded to lower values of λ. At the same time the tips of the MI_n^r lobes shifted towards the higher-λ values with an increase in the density of the system. The situation was completely different when the three-body constraint was considered in one layer. The tips of MI lobes first oscillated and then, after a critical density, followed a trend similar to the one for the hard-core constraint. We further complemented our findings by repeating the calculations in a one-dimensional nonlocally coupled ladder superlattice using the DMRG method and showed that the quantum phase diagrams qualitatively agree with the CMFT method. The physics obtained in this work deals with the system of bosons in two-layer systems with different types of on-site interactions in a superlattice. The results provide a detailed analysis of the effect of constrained bosons on the overall phase diagram of the bilayer system, which is also equivalent to a two-component atomic system. With the experimental progress in controlling local and dipole-dipole interactions in recent years, these findings can be experimentally observed with the existing quantum gas setups.

APPENDIX: EFFECT OF LARGER CLUSTER SIZES

To verify the stability of the phases with respect to the cluster size, in this Appendix we compare our previous results with those obtained using an eight-site bilayer cluster. To this end, first we compare the ρ-μ plots for two representative values of $\lambda = 8.1$ and 18.4, given in Figs. 12(a) and 12(b), respectively. The occupation number density curves obtained using four-site (eight-site) bilayer clusters are marked with dashed line and black squares (solid line and red crosses). It can be clearly seen that the Mott plateaus in both cases largely overlap and are clearly visible. Also, the critical μ/t value changes only slightly. This is the first indication of the stability of the MI phases.

Next we compare the Mott phase boundaries for the densities corresponding to the plateaus shown in Figs. 12(a) and 12(b). For this purpose we plot the MI lobes in the λ-μ plane as shown in Figs. 13(a) and 13(b) and check for the shift in the phase boundaries, if any. The MI lobes obtained using the four-site bilayer cluster are marked by black solid lines and for comparison purposes a few select data points have also been marked with black squares. The data points obtained using the eight-site bilayer cluster are marked with red crosses. The MI lobe in Fig. 13(a) [13(b)] corresponds to the density plateau shown in Fig. 13(a) [13(b)]. It can be seen that the data points overlap very well in both cases and there are no significant changes in the phase boundaries. This holds true near as well as away from the tips of the Mott lobes.

[1] M. Greiner, O. Mandel, T. Esslinger, T. W. Hänsch, and I. Bloch, Nature (London) **415**, 39 (2002).

[2] M. P. A. Fisher, P. B. Weichman, G. Grinstein, and D. S. Fisher, Phys. Rev. B **40**, 546 (1989).

[3] D. Jaksch, C. Bruder, J. I. Cirac, C. W. Gardiner, and P. Zoller, Phys. Rev. Lett. **81**, 3108 (1998).

[4] S. Will, T. Best, U. Schneider, L. Hackermüller, D.S. Lühmann, and I. Bloch, Nature (London) **465**, 197 (2010).

[5] M. J. Mark, E. Haller, K. Lauber, J. G. Danzl, A. J. Daley, and H.-C. Nägerl, Phys. Rev. Lett. **107**, 175301 (2011).

[6] A. J. Daley and J. Simon, Phys. Rev. A **89**, 053619 (2014).

[7] P. R. Johnson, E. Tiesinga, J. V. Porto, and C. J. Williams, New J. Phys. **11**, 093022 (2009).

[8] D. S. Petrov, Phys. Rev. Lett. **112**, 103201 (2014).

[9] D. S. Petrov, Phys. Rev. A **90**, 021601(R) (2014).

[10] B.-l. Chen, X.-b. Huang, S.-p. Kou, and Y. Zhang, Phys. Rev. A **78**, 043603 (2008).

[11] J. Silva-Valencia and A. M. C. Souza, Phys. Rev. A **84**, 065601 (2011).

[12] T. Sowiński, Phys. Rev. A **85**, 065601 (2012).

[13] J. Silva-Valencia and A. M. C. Souza, Eur. Phys. J. B **85**, 161 (2012).

[14] M. Singh, A. Dhar, T. Mishra, R. V. Pai, and B. P. Das, Phys. Rev. A **85**, 051604(R) (2012).

[15] S. Ejima, F. Lange, H. Fehske, F. Gebhard, and K. zu Münster, Phys. Rev. A **88**, 063625 (2013).

[16] T. Sowiński, Cent. Eur. J. Phys. **12**, 473 (2014).

[17] T. Sowiński, R. W. Chhajlany, O. Dutta, L. Tagliacozzo, and M. Lewenstein, Phys. Rev. A **92**, 043615 (2015).

[18] A. J. Daley, J. M. Taylor, S. Diehl, M. Baranov, and P. Zoller, Phys. Rev. Lett. **102**, 040402 (2009).

[19] B. Paredes, A. Widera, V. Murg, O. Mandel, S. Fölling, I. Cirac, G. V. Shlyapnikov, T. W. Hänsch, and I. Bloch, Nature (London) **429**, 277 (2004).

[20] M. A. Baranov, M. Dalmonte, G. Pupillo, and P. Zoller, Chem. Rev. **112**, 5012 (2012).

[21] S. Baier, M. J. Mark, D. Petter, K. Aikawa, L. Chomaz, Z. Cai, M. Baranov, P. Zoller, and F. Ferlaino, Science **352**, 201 (2016).

[22] L. Chomaz, D. Petter, P. Ilzhöfer, G. Natale, A. Trautmann, C. Politi, G. Durastante, R. M. W. van Bijnen, A. Patscheider, M. Sohmen, M. J. Mark, and F. Ferlaino, Phys. Rev. X **9**, 021012 (2019).

[23] L. Tanzi, E. Lucioni, F. Famà, J. Catani, A. Fioretti, C. Gabbanini, R. N. Bisset, L. Santos, and G. Modugno, Phys. Rev. Lett. **122**, 130405 (2019).

[24] F. Böttcher, J.-N. Schmidt, M. Wenzel, J. Hertkorn, M. Guo, T. Langen, and T. Pfau, Phys. Rev. X **9**, 011051 (2019).

[25] C. Trefzger, C. Menotti, and M. Lewenstein, Phys. Rev. Lett. **103**, 035304 (2009).

[26] A. Safavi-Naini, Ş. G. Söyler, G. Pupillo, H. R. Sadeghpour, and B. Capogrosso-Sansone, New J. Phys. **15**, 013036 (2013).

[27] A. Argüelles and L. Santos, Phys. Rev. A **75**, 053613 (2007).

[28] M. Singh, S. Mondal, B. K. Sahoo, and T. Mishra, Phys. Rev. A **96**, 053604 (2017).

[29] J. Catani, L. De Sarlo, G. Barontini, F. Minardi, and M. Inguscio, Phys. Rev. A **77**, 011603(R) (2008).

[30] D. S. Hall, M. R. Matthews, J. R. Ensher, C. E. Wieman, and E. A. Cornell, Phys. Rev. Lett. **81**, 1539 (1998).

[31] S. Trotzky, P. Cheinet, S. Fölling, M. Feld, U. Schnorrberger, A. M. Rey, A. Polkovnikov, E. A. Demler, M. D. Lukin, and I. Bloch, Science **319**, 295 (2008).

[32] R. Jördens, N. Strohmaier, K. Günter, H. Moritz, and T. Esslinger, Nature (London) **455**, 204 (2008).

[33] A.-C. Voigt, M. Taglieber, L. Costa, T. Aoki, W. Wieser, T. W. Hänsch, and K. Dieckmann, Phys. Rev. Lett. **102**, 020405 (2009).

[34] M. Snoek, I. Titvinidze, I. Bloch, and W. Hofstetter, Phys. Rev. Lett. **106**, 155301 (2011).

[35] K. Günter, T. Stöferle, H. Moritz, M. Köhl, and T. Esslinger, Phys. Rev. Lett. **96**, 180402 (2006).

[36] G. Roati, F. Riboli, G. Modugno, and M. Inguscio, Phys. Rev. Lett. **89**, 150403 (2002).

[37] T. Best, S. Will, U. Schneider, L. Hackermüller, D. van Oosten, I. Bloch, and D.-S. Lühmann, Phys. Rev. Lett. **102**, 030408 (2009).

[38] A. Richaud and V. Penna, Condens. Matter **5**, 2 (2020).

[39] L. He, Y. Li, E. Altman, and W. Hofstetter, Phys. Rev. A **86**, 043620 (2012).

[40] F. Hébert, G. G. Batrouni, X. Roy, and V. G. Rousseau, Phys. Rev. B **78**, 184505 (2008).

[41] T. Mishra, R. V. Pai, and B. P. Das, Phys. Rev. A **76**, 013604 (2007).

[42] T. Mishra, B. K. Sahoo, and R. V. Pai, Phys. Rev. A **78**, 013632 (2008).

[43] T. Ozaki and T. Nikuni, J. Phys. Soc. Jpn. **81**, 024001 (2012).

[44] H. Pu and N. P. Bigelow, Phys. Rev. Lett. **80**, 1130 (1998).

[45] A. Kuklov, N. Prokof'ev, and B. Svistunov, Phys. Rev. Lett. **92**, 050402 (2004).

[46] L. Mathey, Phys. Rev. B **75**, 144510 (2007).

[47] A. Isacsson, M.-C. Cha, K. Sengupta, and S. M. Girvin, Phys. Rev. B **72**, 184507 (2005).

[48] S. Sugawa, K. Inaba, S. Taie, R. Yamazaki, M. Yamashita, and Y. Takahashi, Nat. Phys. **7**, 642 (2011).

[49] H. Hara, H. Konishi, S. Nakajima, Y. Takasu, and Y. Takahashi, J. Phys. Soc. Jpn. **83**, 014003 (2014).

[50] S. Peil, J. V. Porto, B. Laburthe Tolra, J. M. Obrecht, B. E. King, M. Subbotin, S. L. Rolston, and W. D. Phillips, Phys. Rev. A **67**, 051603(R) (2003).

[51] J. Sebby-Strabley, M. Anderlini, P. S. Jessen, and J. V. Porto, Phys. Rev. A **73**, 033605 (2006).

[52] M. Singh and T. Mishra, Phys. Rev. A **94**, 063610 (2016).

[53] A. Dhar, T. Mishra, R. V. Pai, and B. P. Das, Phys. Rev. A **83**, 053621 (2011).

[54] A. Dhar, M. Singh, R. V. Pai, and B. P. Das, Phys. Rev. A **84**, 033631 (2011).

[55] A. Dhar, T. Mishra, R. V. Pai, S. Mukerjee, and B. P. Das, Phys. Rev. A **88**, 053625 (2013).

[56] R. Roth and K. Burnett, Phys. Rev. A **68**, 023604 (2003).

[57] F. Schmitt, M. Hild, and R. Roth, Phys. Rev. A **80**, 023621 (2009).

[58] G. Roux, T. Barthel, I. P. McCulloch, C. Kollath, U. Schollwöck, and T. Giamarchi, Phys. Rev. A **78**, 023628 (2008).

[59] P. Cheinet, S. Trotzky, M. Feld, U. Schnorrberger, M. Moreno-Cardoner, S. Fölling, and I. Bloch, Phys. Rev. Lett. **101**, 090404 (2008).

[60] F. Grusdt, M. Höning, and M. Fleischhauer, Phys. Rev. Lett. **110**, 260405 (2013).

[61] S. Nascimbène, Y.-A. Chen, M. Atala, M. Aidelsburger, S. Trotzky, B. Paredes, and I. Bloch, Phys. Rev. Lett. **108**, 205301 (2012).

[62] E. Altman, W. Hofstetter, E. Demler, and M. D. Lukin, New J. Phys. **5**, 113 (2003).

[63] B.-L. Chen, S.-P. Kou, Y. Zhang, and S. Chen, Phys. Rev. A **81**, 053608 (2010).

[64] K. Sheshadri, H. Krishnamurthy, R. Pandit, and T. Ramakrishnan, Europhys. Lett. **22**, 257 (1993).

[65] I. Danshita, J. E. Williams, C. A. R. Sá de Melo, and C. W. Clark, Phys. Rev. A **76**, 043606 (2007).

[66] Y.-C. Chen and M.-F. Yang, J. Phys. Commun. **1**, 035009 (2017).

[67] B. Yang, H.-N. Dai, H. Sun, A. Reingruber, Z.-S. Yuan, and J.-W. Pan, Phys. Rev. A **96**, 011602(R) (2017).

[68] M. Lewenstein, L. Santos, M. A. Baranov, and H. Fehrmann, Phys. Rev. Lett. **92**, 050401 (2004).

[69] P. Donohue, M. Tsuchiizu, T. Giamarchi, and Y. Suzumura, Phys. Rev. B **63**, 045121 (2001).

[70] A. E. Feiguin and M. P. A. Fisher, Phys. Rev. B **83**, 115104 (2011).

[71] F. Crépin, N. Laflorencie, G. Roux, and P. Simon, Phys. Rev. B **84**, 054517 (2011).

[72] M. Okumura, S. Yamada, M. Machida, and H. Aoki, Phys. Rev. A **83**, 031606(R) (2011).

[73] C. Degli Esposti Boschi, A. Montorsi, and M. Roncaglia, Phys. Rev. B **94**, 085119 (2016).

[74] W.-L. Liu, T.-Z. Yuan, Z. Lin, and W. Yan, Chin. Phys. B **28**, 020303 (2019).

[75] T. Giamarchi, *Quantum Physics in One Dimension* (Clarendon, Oxford, 2003), Vol. 121.

[76] M. Fabrizio, A. Parola, and E. Tosatti, Phys. Rev. B **46**, 3159 (1992).

[77] N. Nagaosa, Solid State Commun. **94**, 495 (1995).

[78] H. J. Schulz, Phys. Rev. B **53**, R2959 (1996).

[79] L. Balents and M. P. A. Fisher, Phys. Rev. B **53**, 12133 (1996).

[80] R. M. Noack, S. R. White, and D. J. Scalapino, Physica C **270**, 281 (1996).

[81] S. R. White, I. Affleck, and D. J. Scalapino, Phys. Rev. B **65**, 165122 (2002).

[82] P. Donohue and T. Giamarchi, Phys. Rev. B **63**, 180508(R) (2001).

[83] M. S. Luthra, T. Mishra, R. V. Pai, and B. P. Das, Phys. Rev. B **78**, 165104 (2008).

[84] M. Singh, T. Mishra, R. V. Pai, and B. P. Das, Phys. Rev. A **90**, 013625 (2014).

[85] E. Orignac and T. Giamarchi, Phys. Rev. B **64**, 144515 (2001).

[86] M. A. Cazalilla, A. F. Ho, and T. Giamarchi, New J. Phys. **8**, 158 (2006).